Ultrastrong Coupling of $Si_{1-x}Ge_x$ Parabolic Quantum Wells to Terahertz Microcavities

Fritz Berkmann,[†] Tommaso Venanzi,[†] Leonetta Baldassarre,[†] Elena Campagna,[‡] Enrico Talamas-Simola,[‡] Luciana Di Gaspare,[‡] Cedric Corley-Wiciak,[¶,§] Giovanni Capellini,[¶,‡] Giuseppe Nicotra,[∥] Gianfranco Sfuncia,[∥] Andrea Notargiacomo,[⊥] Ennio Giovine,[⊥] Sara Cibella,[⊥] Michele Virgilio,[#] Giacomo Scalari,[@] Monica De Seta,[‡] and Michele Ortolani[*,†]

†*Department of Physics, Sapienza University of Rome, Rome, Italy*

‡*Department of Science, Roma Tre University, Rome, Italy*

¶*IHP - Leibniz-Institut für innovative Mikroelektronik, Frankfurt(Oder), Germany*

§*European Synchrotron Radiation Facility, Grenoble Cedex 9, France*

∥*Institute for Microelectronics and Microsystems IMM-CNR, Catania, Italy*

⊥*Institute for Photonics and Nanotechnologies IFN-CNR, Rome, Italy*

#*Department of Physics, University of Pisa, Pisa, Italy*

@*Institute of Quantum Electronics, Eidgenössische Technische Hochschule Zürich, Switzerland*

E-mail: michele.ortolani@roma1.infn.it

Abstract

Control and manipulation of quantum states by light is increasingly important for both fundamental research and applications. This can be achieved through the strong coupling between light and semiconductor devices, typically observed at THz frequencies in 2D electron gases embedded in lithographic optical cavities. Here we explore the possibility of achieving ultrastrong coupling between conduction sub-band states in $Si_{1-x}Ge_x$ heterostructures and THz cavity photons fabricated with a potentially silicon-CMOS-compliant process. We developed $Si_{1-x}Ge_x$ parabolic quantum wells with transition at $\omega_0 = 3.1$ THz and hybrid metal-plasmonic THz patch-antenna microcavities resonating between 2 and 5 THz depending on the antenna length. In this first demonstration we achieved anti-crossing around 3 THz with spectroscopically measured Rabi frequency $\Omega_R \simeq 0.7$ THz ($\Omega_R/\omega_0 \simeq 0.2$ i.e. ultrastrong coupling). The present group-IV semiconductor material platform can be extended to the 5-12 THz range, where these semiconductors are transparent, as opposed to the III-V compound semiconductors plagued by strong THz optical phonon absorption. Moreover, the intersubband transition in parabolic quantum wells hosted by the non-polar $Si_{1-x}Ge_x$ crystal lattice is robust against carrier density and temperature variations, making the strength of the coupling only weakly temperature-dependent from 10 to 300 K. These results pave the way for the employment of the $Si_{1-x}Ge_x$ material platform to perform fundamental research in ultrastrong light-matter coupling, fully exploiting the plasmonic character of the cavity mirror, as well as in ultrafast modulators and saturable absorbers for THz laser research.

Introduction

The strong coupling regime of the light-matter interaction has been recently reported in many different physical systems[1] and electromagnetic frequency ranges from the microwaves,[2,3] to the terahertz,[4–7] the infrared[8,9] and the visible.[10,11] Strong coupling appears when a quantum system, showing a spectrally isolated "matter" resonance, modeled with a two-level system with transition energy $\hbar\omega_0$, is embedded into an electromagnetic cavity featuring its own "light" resonance at frequency ω_c. Experimentally, the strong coupling regime is detected through the spectroscopic observation of polariton band dispersion as a function of detuning

$(\omega_0 - \omega_c)$ controlled by the cavity length,[6,7,9,12] by an external field,[4,13–15] or by temperature T.[16] Anti-crossing behavior of light and ”matter” resonances is then observed, and the light-matter coupling strength can be quantitatively assessed by measuring the frequency difference between the upper and lower polariton bands at zero detuning, corresponding to twice the Rabi frequency Ω_R of the ideal two-level system.[17] Perspective applications of this phenomenon rely on the mixed light-matter nature of polaritons, which would eventually allow the control of quantum light through degrees of freedom that are typically employed to control quantum matter, such as electron or spin currents, and electric or magnetic fields. In this respect, lithographic semiconductor microcavities that feature high reproducibility, scalability of the production, and possible room-T operation[6,7,18–20] may be favored over more exotic materials and configurations. The use of foundry-compatible epitaxial semiconductor layers is also a clearly desirable feature for applications. This is even more desirable if the material is silicon-based and/or compatible with silicon foundry technology. Especially a material compatibility with the CMOS processes and post-processing, such as in Ge and for SiGe alloys is of great advantage.[21]

Indeed, semiconductor quantum wells (QWs) supported by epitaxial semiconductor heterostructures have been consistently used in the realization of strong-coupling system due to the possibility of designing two-level-like resonances with ω_0 in the mid-IR and THz ranges and strong transition dipole moment μ_{12} set by the highly confined 2D (two-dimensional) electron density n_{2D}, to be employed as the “matter” oscillator. The cyclotron resonance of a 2D electron gas (2DEG) confined in a QW can be strongly coupled to a 2D metasurface of metallic split-ring resonators acting as cavities.[4,14] In general, 2DEG resonances benefit from collective coupling enhancement because the 2DEG acts as a single quantum system,[22] therefore the normalized coupling-strength ratio Ω_R/ω_0 scales with $\sqrt{n_{2D}}$, as outlined in the seminal paper from Dicke.[23] Furthermore, n_{2D} can be increased by remote (modulation) doping without increasing the QW volume or the energy loss. Another type of QW resonances, not requiring a magnetic field, however with lower quality factor than cyclotron resonances, are intersubband transitions (ISBTs) between quantum-confined states in the well (subbands). After the initial demonstration in a dielectric cavity,[24] the use of sub-wavelength metal-bound microcavities and the progressive scaling of ω_0 towards THz frequencies led to intriguing demonstrations of ultrastrong light-matter coupling, where $\Omega_R/\omega_0 > 0.1$.[17,19] The collective nature of ISBTs, effectively constituting a plasmon,[22] has been theoretically described using the dipolar gauge,[25] showing interesting interplay between the strong coupling and the depolarization shift that poses as well some limitations to the normalized coupling strength.[7,26]

Theoretically, the light-matter coupling constant Ω_R is given by the matter transition rate due to the excitation by cavity vacuum field fluctuations. If one assumes a homogeneous average vacuum field strength E_{vac} in a cavity filled with a lossless medium with dielectric constant ε, one can write:[1,17,27]

$$\Omega_R = \frac{\mu_{12} E_{vac}}{\hbar} = \frac{\mu_{12}}{\hbar}\sqrt{\frac{\hbar\omega_0}{2\varepsilon_0\varepsilon V_m}} = \sqrt{\frac{f_{12}e^2}{\varepsilon_0\varepsilon m^*}\frac{N_{QW}}{L}n_{2D}} \tag{1}$$

where we have first written E_{vac} in terms of the ratio of the transition energy $\hbar\omega_0$ over the cavity modal volume ϵV_m, and then we have further specified μ_{12} in the relevant case of a 2DEG at zero temperature embedded in a planar cavity of length L using the oscillator strength f_{12}, the electron effective mass m^*, and the fundamental charge e. The integer number $N_{QW} \geq 1$ comprises the stacking of many identical epitaxial layers with identical 2DEGs in the same cavity with homogeneous field, assuming total filling of the cavity with QWs. It turns out that ISBTs with high μ_{12} due to high n_{2D}, embedded in microcavities with nanometric L (and therefore V_m) hence very high E_{vac}, provide light-matter coupling values Ω_R/ω_0 among the largest of all physical systems.[1] In previous work on the strong coupling of ISBTs to cavities, the focus was mostly on the cavity design, trying to minimize V_m,[18,28,29] or to obtain a cavity field perfectly parallel to the dipole moment of ISBTs (orthogonal to the epitaxial plane), which has been achieved in patch antennas with a metallic ground plane,[6,30,31] in double-metal gratings[9] and in fully etched metal-insulator-metal (MIM) cavities.[32] A two-level "matter" oscillator spectrum is provided by QWs with parabolic confinement potential (PQWs) that mirrors a quantum harmonic oscillator, in which empty-band excited states are equidistant in energy.[33,34] Therein, the Kohn's theorem guarantees that the Hartree interaction term is exactly canceled out by the many-body corrections, therefore the ISBT energy does not depend any more on the electron population. Strong coupling at THz frequencies has been observed in III-V compound-semiconductor PQWs grown by many small steps of digital alloying,[7] and, more recently, in extremely high-quality III-V PQWs[34] obtained by continuous variation of the alloy composition[19] .

In this work we further develop $Si_{1-x}Ge_x$ PQWs with continuously graded alloy profile[35,36] and we embed them into suitable microcavities (fully-etched patch-antennas, or MIM resonators) to observe the strong coupling at THz frequencies in a group-IV, silicon foundry-compatible, material. One of the mirrors of MIM resonators is realized with a heavily doped semiconductor layer instead of a metallic layer to allow future fabrication in silicon foundries. Ultrastrong coupling with $\Omega_R/\omega_0 \simeq 0.2$ is achieved. The ultrastrong coupling condition is observed up to room-T, with quality factor of the polariton spectral lines almost independent on T, which is attributed to the weaker electron-phonon interaction featured by the non-polar lattice of group IV semiconductors, if compared to the polar III-V compound semiconductors. The coupling strength also has a very weak dependence on T, which is entirely attributed to the variation with T of the SiGe dielectric constant and of the electron density transferred in the wells from remote dopants, and not to intrinsic properties of the light-matter interaction. The present understanding of the strong-coupling conditions in $Si_{1-x}Ge_x$ quantum wells may be exploited in the future to obtain photonic quantum state manipulation at room-T together with microelectronics integration in silicon-based devices.

Results and discussion

In an ideal PQW, mimicking a collective quantum harmonic oscillator, the spectral weight of ISBTs is concentrated in a single absorption peak, irrespective of the Fermi energy (doping level) and the temperature.[34] The frequency position of this peak can be estimated from the bare energy distance between any two subsequent levels in the undoped parabolic well

$$\Delta E = \hbar\sqrt{\frac{8\Delta_0}{W^2 m_z^*}} \tag{2}$$

where Δ_0 is the energy difference between the minimum of the undoped PQW and its edge, where the constant-composition barrier for electrons starts on both sides of the well (barrier height, set by the maximum band offset of the heterostructure), W is the total well width of the order of tens of nanometers, and ${m^*}_z$ is the electron-confinement effective mass in the growth direction z. In Figure 1 we show the schematics of the complete heterostructure, which consists of a superlattice of 25 PQWs realized on a GeSi/Ge virtual substrate (VS) grown on silicon substrate wafers. The PQW heterostructure has been grown epitaxially by ultra-high vacuum chemical vapor deposition (UHV-CVD) using GeH_4 and SiH_4 gas precursors, without carrier gas.[35] The first layer of the VS consists of a relatively thick (3 µm) Ge buffer layer grown directly on the Si(001) wafer substrate by means of an out-of-equilibrium growth technique,[37] which allows to completely relax the heteroepitaxial strain existing with the underlying Si substrate, while minimizing the density of extended defects generated during the plastic relaxation process, such as the threading dislocations.[38] A 2000-nm thick, reverse-graded concentration $Si_{1-x}Ge_x$ layer is then grown to achieve a lattice parameter a corresponding to that of a relaxed $Si_{0.10}Ge_{0.90}$ alloy. This particular composition is chosen to realize the strain compensation conditions for the PQW active layer. The PQWs are grown by continuously varying the gas precursor concentration in the CVD reactor to obtain a composition profile of ideal parabolic wells of thickness $W = 61$ nm, reaching a Ge content $x = 1$ at the center of the wells and $x = 0.82$ at the inter-well barriers of thickness $b = 16$

nm. Modulation doping with electrons of the PQWs is achieved by remote-impurity doping via PH_3 codeposition in the central region of the barriers. Modulation doping is possible because the ionized phosphorus impurity states are of higher energy than the ground state of the PQW, and thus electrons are transferred in the donor-free well region. A scanning transmission electron microscopy (STEM) image of a typical sample is shown in Figure 1(a), where one can see the high quality of the structure and the absence of extended defects. In Figure 1(b) we display a highly resolved STEM detail of the structure with the composition profile overlaid, as obtained by the calibration of the STEM intensity profile with the secondary ion mass spectroscopy (SIMS) data. The high reproducibility of the PQW epitaxial deposition process is clearly evident in Figure 1(c), where the individual SIMS-calibrated STEM intensity profiles of 10 PQWs of the stack are superimposed and plotted together with the nominal parabolic composition profile. The high accuracy obtained in the profile of each PQW can be quantified by the relative composition profile error displayed at the bottom of panel c, showing that the grown composition profile agrees with the nominal one within 1%, for all the measured PQWs. The high reproducibility of the 25-PQW superlattice (SL) is also confirmed by x-ray diffraction (XRD) data in Figure 1(d), showing sharp SL peaks and a very good agreement between the simulation of the 004 Bragg reflection XRD scan (black curve) and the experimental data (green curve). The XRD measurement also confirms the lattice matching of the VS and the PQWs. This thorough characterization of the heterostructure enabled us to properly calculate the electronic states of the PQWs. In Figure 1(e) we report the bare energy profile determined by means of a multi-valley self-consistent code in the parabolic $\mathbf{k} \cdot \mathbf{p}$ envelope function approximation[39] using the parabolic Ge composition x profile measured by SIMS/STEM as input. The resulting real potential shape (black curve in panel (e)) is very close to an ideal parabola with $\Delta_0 = 112$ meV and $W = 61$ nm. Consequently, using $m_z^* = 0.13\ m_e$ for the Ge conduction band minimum at the L-point, the associated confined electron states exhibit equally spaced energy separation $\Delta E = 12$ meV. In Figure 1(f) we report the effective energy band profile at 10 K accounting for the Hartree potential in the case of the doped well, at the doping level used in this work. Note that, although the energy level spacing decreases if compared to the undoped case, the ISBT energy $\hbar\omega_0$ is still expected at the undoped value ΔE according to the Kohn's theorem.[17]

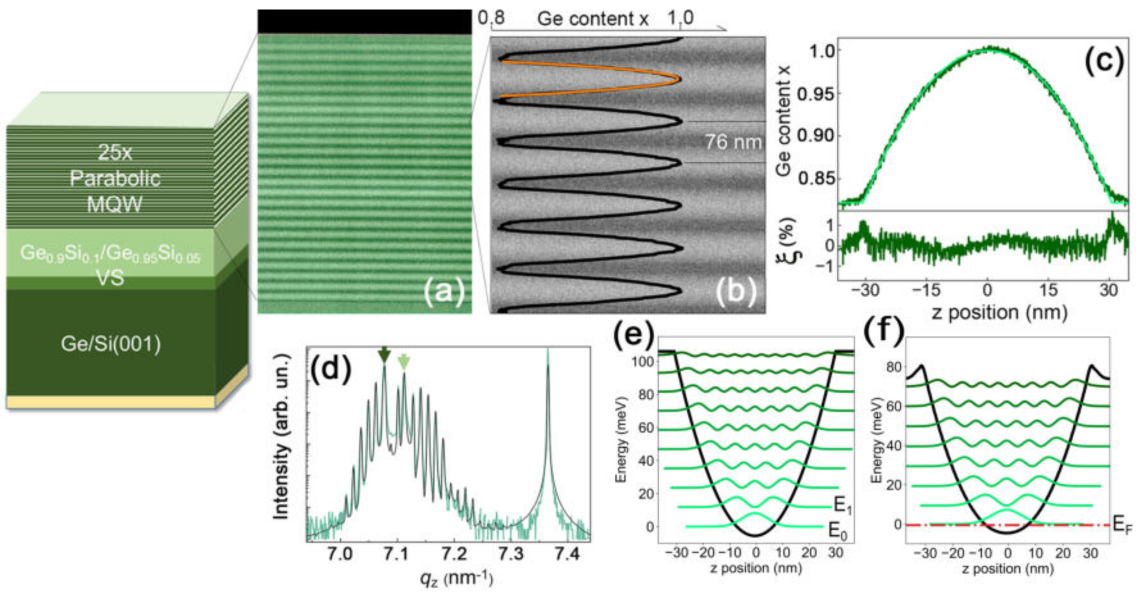

Figure 1: Schematics of the grown heterostructure together with (a) False color dark-field STEM image of the entire PQW stack. Lighter green corresponds to higher Ge content. (b) STEM details of the PQWs stack overlaid by the composition profile obtained by SIMS-calibrated STEM. (c) Top: Superposition of ten different PQW STEM profiles (dark green) and of the nominal parabolic concentration profile (light green). Bottom: relative composition error for all the ten PQW composition profiles. (d) XRD curve across the 004 Bragg reflection of the heterostructure. With dark/light green arrows we identify the diffraction signals from the thick Ge buffer layer and $Si_{0.1}Ge_{0.9}$ VS, respectively. (e) Calculated confinement energy profile at the L point of the conduction band for an undoped PQW having the compositional parabolic profile shown in (c) (black) together with the square modulus of the wavefunctions, that are plotted at the energy level of the corresponding quantized state, using $m_z^* = 0.13\ m_e$ for electrons at the L-point of the conduction band of Ge. (f) Same as (e) for the doped PQW used in this work. The dash-dotted line represents the Fermi level for the nominal doping density. The calculations have been preformed at 10 K

The matter resonance frequency ω_0 was then measured by performing ISBT spectroscopy with a Fourier-transform infrared spectrometer (FTIR) adapted to work in the THz range (1-30 THz) (see setup sketch 2(b)), in vacuum and at temperatures T from 10 K to 300 K, in linear-dichroism mode, and in transmission configuration with small focal spot of the order of the wafer thickness (0.5 mm). Samples with doped PQWs were metal-coated and cut into side-coupled prism waveguides to probe the ISBT absorption in the volume occupied by the PQWs, as sketched in Figure 2(c). ISBT spectra are calculated after baseline subtraction of linear-dichroic ratios at several T and reported in Figure 2(a). A single strong transmission dip at all T is the signature of a harmonic-oscillator absorption spectrum, better described as a collective "bosonic matter" excitation.[17] From a global fitting of the data in Figure 2(a) with an exponentially modified Gaussian function (see Supporting Information for the fitting curves), we measured the center absorption frequency $\omega_0 = 3.1 \pm 0.2$ THz at all T. A numerical estimate of n_{2D} in the PQWs was obtained by solving the multi-valley self-consistent Schrödinger-Poisson equations for the actual charge transfer of electrons from remote (modulation) dopant impurities in the barriers to the wells. This calculation also allows to predict the Fermi level position for the used doping density at 10 K, reported in Figure 1(f). Due to the high density of states at the bottom of the conduction band of Ge, the Fermi level does not considerably shift above the ground state with increasing doping, even in the present case of moderately high doping, at odds with most III-V compound semiconductor PQWs. We estimate $n_{2D} \sim 3 \times 10^{11}$ cm^{-2}, in reasonable agreement with the corresponding values estimated by the ISBT absorption spectral weight measured from Figure 2(a)[39] that however has high uncertainty levels at all Ts. The lowest linewidth is observed at 100 K, from which we estimate an energy loss parameter of the "matter" resonance $\Gamma_{\mathrm{ISBT}} = 1.0$ THz, rising to 1.7 THz at room-T mostly due to the electron-phonon interaction. At $T < 100$ K, Γ_{ISBT} increases again, as already observed in modulation-doped rectangular Ge/$Si_{1-x}Ge_x$ QWs,[40] where this effect has been attributed to the interplay between the ionized impurity density and the electron kinetic energy both varying with T as also observed in III-V compound semiconductor PQWs.[41]

For the cavity design we have chosen a square patch antenna with conducting ground plane and etched sidewalls, to improve the field confinement inside the cavity. Patch antennas have been employed successfully in mid-IR and THz strong coupling experiments with ISBTs

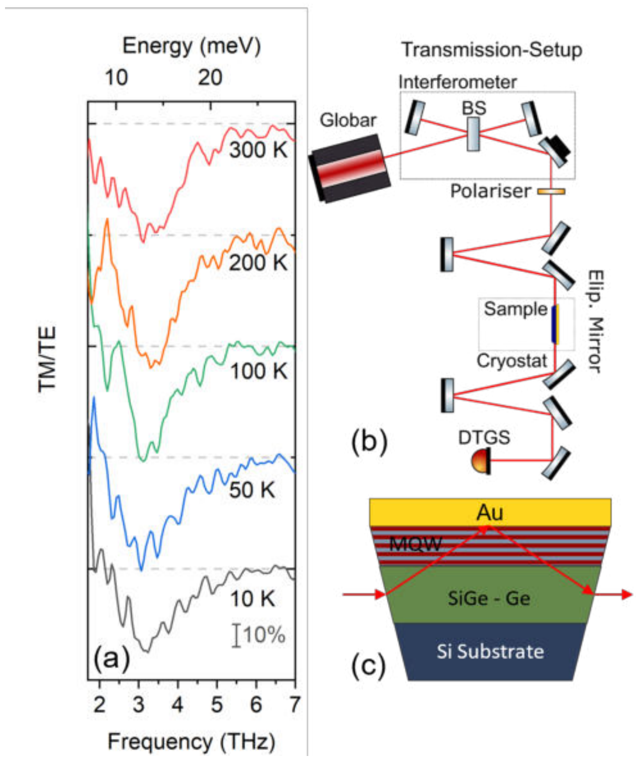

Figure 2: FTIR spectroscopy characterization of the specific PQW structure used in this work. (a) Linear-dichroic transmission spectra at various temperatures, from $T = 10$ K to room-temperature. (b) Sketch of the optical beam path and (c) sketch of the sample in the prism waveguide geometry.

in QWs.[6,30–32] The optimal cavity length L for increasing the vacuum field and therefore the light-matter interaction strength, given by the distance between the conducting ground plane and the top metal patch directly evaporated on the last layer of the heterostructure, has been determined in Ref.[42] from electromagnetic (EM) simulations to be between 1.5 and 2.0 µm. Therefore, a value of $L = 1.8$ µm was chosen after performing similar EM simulations with 3D finite-element commercial software (CST microwave studio, see Methods for details) for our group-IV material system using $\varepsilon_\infty = 15.5$ for $Si_{0.10}Ge_{0.90}$ corresponding to the average Ge concentration in the active region. In the simulations of Figure 3(c-e), the square patch side s has been varied from 7 µm to 14 µm to span the cavity resonance frequency range $\omega_c = 2.0$ to 4.5 THz encompassing the $\omega_0 = 3.1$ THz determined from Figure 2: the predicted crossing is found at $s = 13$ µm for a MIM cavity (yellow curve in Figure 3(c)). A large-area periodic array is typically required for far-field optical experiments on microcavities: here, the period P of the square array of patch antennas was set to $P = 3s$ to avoid dipole coupling among neighboring patches. For example, Todorov et al.[6,25] have studied the strong coupling in similar THz square microcavity arrays, however in the limit where the spacing between patches is smaller than s, $P < 2s$. Therein, both P and s influence the optical absorption resonance frequency, while in this work we seek a condition where the spectral position of ω_c is independent from P.[28,30,31]

In order to make the fabrication process potentially compatible with CMOS foundries, and to eventually exploit plasmonic effects at shorter wavelengths in the future, we adopt a cavity configuration where the lower metallic mirror is replaced by an highly doped semiconductor ground plane. The ground plane was realised by heavily doping the reverse-graded $Si_{1-x}Ge_x$ virtual substrate (light green layer in Figure 1) and characterized experimentally in a separate area of one of the samples, where the PQW heterostructure was fully etched away. The dielectric function of the n^+-SiGe alloy (average composition $Si_{0.05}Ge_{0.95}$) acting as ground plane was determined by measuring its absolute reflectance in the 1-100 THz range by FTIR spectroscopy for $T = 10$ K and $T = 300$ K with a gold mirror reference (Figure

3(a)), and then applying Kramers-Kroning transformations.[43] The results are shown in Figure 3(b): the screened plasma frequency is found at 16 THz at both temperatures, which is not as high as record values for pure Ge of Refs.[43,44] but is high enough for ground-plane operation in the range up to 12 THz (see Figure 3). One may notice the relevant value $\varepsilon' = -175$ at 3 THz at 10 K. The 3D free electron density $n = 6.5 \times 10^{18}$ cm^{-3} , estimated with the Drude model of the reflectance ($m^* = 0.13 m_e$), is well beyond the Mott transition to a degenerate semiconductor, ensuring that the ground plane will have conducting behavior at low T.[43] The calculated skin depth is around 1 µm, half the value of the doped layer thickness of 2 µm.

The measured n$^+$-Si$_{1-x}$Ge$_x$ dielectric function at 300 K was then used to simulate the hybrid metal-insulator-doped semiconductor cavities. From the simulation, the optical overlap compared to identical MIM cavities changed by less than 5% over the considered frequency range. The spectral results for the cavity with undoped PQW filling are shown in Figure 3(d). The quality factors (Figure 3(g)) are now dominated by losses in the ground plane but they are still better than the ISBT quality factor, so it is not expected that this will be the dominant loss factor in the final device with doped PQWs. The linear dependence (Figure 3(f)) of ω_c vs. s^{-1} found in MIM cavities of Figure 3(c) is confirmed, with a global redshift of $\sim$ 1.5 THz, indicating that a larger area of the ground plane is involved in the EM current patterns compared to the gold ground plane.[28] The predicted crossing is now found at $s = 10$ µm for the hybrid cavity. The absolute value of the absorption decreases for longer s and lower ω_c due to increasing mismatch between the wavelength and L.[45] Finally, the strong-coupling conditions were simulated by introducing an anisotropic dielectric function for the doped PQW layer (Figure 3(h)).[46] The dielectric function parameters are calculated from the ISBT spectra in Figure 2 and we added an optical overlap factor $f_{\mathrm{QW}} = 0.29$ that measures the cavity volume effectively occupied by the 2D-confined electrons at $T = 10$ K as further explained below.[19] A clear splitting of the polariton dispersion as a function of s is observed in Figure 3(e), with the lower polariton much less intense than the upper polariton, due to the above-mentioned mismatch between the wavelength and L.[45] Nevertheless, transfer of spectral weight from the upper to the lower polariton is observed, as expected, when approaching the predicted crossing. The numerical estimate of the Rabi frequency, determined from half the splitting at 10 µm, is $\Omega_R = 0.55$ THz, which is comparable to both the "light" and the "matter" loss parameters around 1 THz estimated from Figure 3(d) and Figure 2(a), respectively. Knowing what to expect, we can now proceed with the experimental demonstration.

The cavity array fabrication was performed by electron-beam lithography and reactive-ion etching (see Methods for details). Two nominally identical samples featuring both the plasmonic ground plane and the doped PQW stack were used, as well as a a third identical sample with undoped PQW stack. The PQW epitaxial stack was kept identical to that of the samples analyzed in Figures 1 and 2, with the only difference of the heavy doping of the n^+-$Si_{1-x}Ge_x$ virtual substrate. Cavities with different s spanning the $7-14$ µm range around the predicted crossing at $s = 10$ µm were simultaneously fabricated on the same chip in the same nanofabrication process, ensuring that the cavity walls, the etching depth and the heterostructure parameters were exactly the same for all values of s. For the first sample a pitch of $P = 2s$ was used while for the second and third (undoped) sample a pitch of $P = 3s$ was used to experimentally check for possible effects of interacting cavities. Two electron microscopy images of the first sample after cavity fabrication are shown in Figure 4(c,d), also showing the experimental definition of s and P. Each array was 2×2 mm^2 in size, spaced by 1 mm. A 2×2 mm^2 area without cavities was etched down to the ground plane and used as the reflectance reference for the polariton spectroscopy experiment in the 1-6 THz range. These "empty arrays" were also used for the measurements in Figure 3(a,b).

Cavity reflectance spectra $R(\omega)$ can be considered as the opposite of absorption spectra $A(\omega) = 1 - R(\omega)$ due to the presence of the ground plane that prevents any transmittance.[6,19] For the reflectance measurements we developed a custom-made optical insert based on tightly-focusing ellipsoidal mirrors (sketched in Figure 5(c)) that could de-magnify

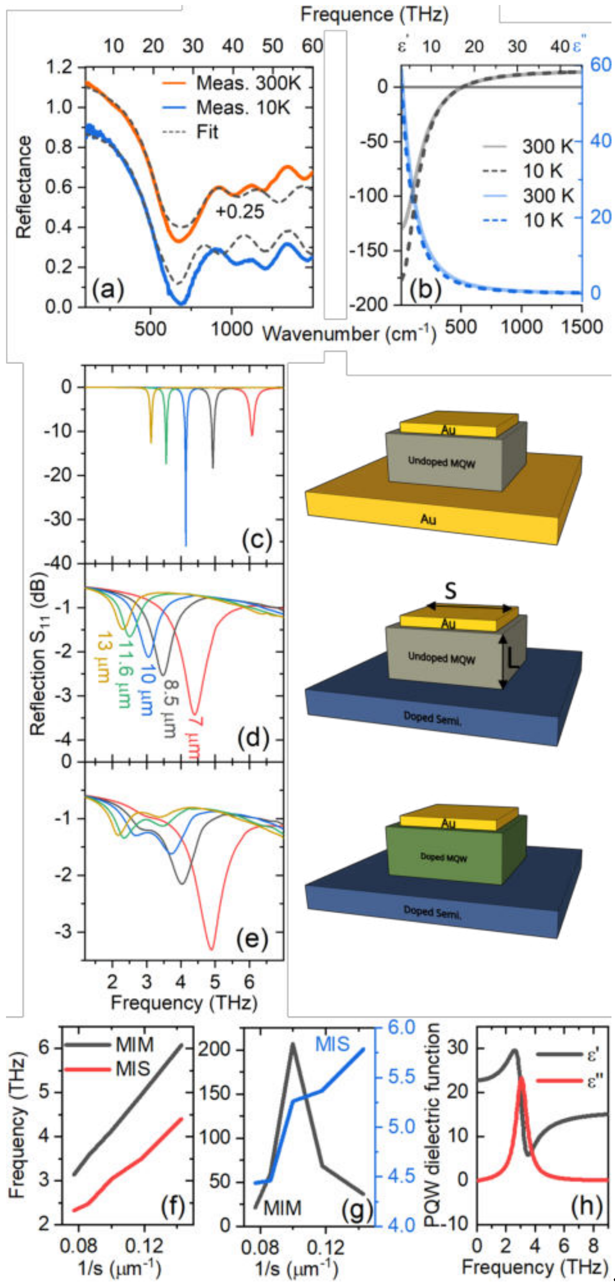

Figure 3: (a) Normal-incidence reflectance with Drude fit and (b) the corresponding dielectric function of the heavily doped $Si_{0.1}Ge_{0.9}$ ground plane. (c-e) Simulated reflection spectra (S_{11} parameter) of microcavities with different gold patch side s as indicated in panel (d) for different color curves. Panel (c): ideal case of a gold ground plane; Panels (d,e): heavily doped $Si_{0.1}Ge_{0.9}$ ground plane with active layer made of (d) undoped and (e) doped PQWs with filling fraction $f_{\mathrm{QW}} = 0.29$. Two polariton branches are apparent in panel (e) with avoided crossing of the intrinsic PQW resonance set at $\omega_0 = 3.1$ THz in the simulations. Note the global resonance redshift and broadening between (c) and (d), and the smaller blueshift of the upper polariton in (e) if compared to the bare cavity resonance in (d), entirely due to the ultrastrong light-matter coupling. (f) Geometry dependence of the resonance position for the MIM (c) and MIS (d) cavities. (g) Q-Factor of the MIM and MIS resonances over the inverse cavity lemgth. (h) used dialectic function for the PWQ simulation

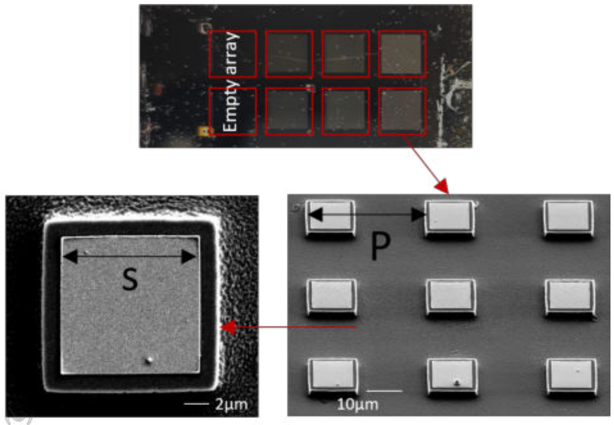

Figure 4: Top: optical image of the 1×2 cm epitaxial chip: six 2×2 mm^2 fields are visible, each of them with cavities of different s. Right: A portion of an array of patch cavities with a unit cell dimension $P = 3s$; note the semiconductor ground plane contrasted to the gold square patch. Left: detail of an individual patch cavity with $s = 11\,\mu$m, where s is the width of the metallic patch.

the FTIR spot size by 3× inside the vacuum chamber of the spectrometer. With this insert, all cavity arrays with different s could be investigated in the same cryogenic cycle, thereby ensuring identical conditions for all spectra in Figure 5(a,b). The reflection spectra of the cavity arrays filled with undoped PQW stack are reported in Figure 5(a,b) for $T = 10$ K (grey curves, identical in the two panels) and are consistent with the simulations in Figure 3(d). Turning to the polariton dispersion at $T = 10$ K (red curves for $P \sim 2s$ in Figure 5(a) and black curves for $P \sim 3s$ in Figure 5(b)), already at $s = 7\,\mu$m with large detuning $\omega_c - \omega_0 \simeq 1.4$ THz, one sees a clear offset in the absorption resonance frequency of the doped-PQW samples, which is due to the upper polariton dispersion being pushed away from the bare cavity value by ultrastrong coupling. Even at $s = 7\,\mu$m the linewidth of the upper polariton is above 1 THz, broader than that of the bare cavity resonance ($\Gamma_c = 0.9$ THz at $\omega_c = 4.5$ THz leading to a typical bare patch antenna Q-factor of 5, decreasing to ~ 4 for doped PQWs). This indicates that electrons in the PQWs contribute to cavity losses. When the cavity resonance is tuned closer to ω_0 ($s > 10\,\mu$m), a splitting in the polariton dispersion is observed, with both upper and lower polariton clearly visible from $s = 11\,\mu$m to $14\,\mu$m. Here, the linewidths of both polaritons are much broader than those of the bare cavity resonances (Q-factors below 3), approaching the limit value $\Gamma_{\text{ISBT}}(10\,\text{K}) = 1.4$ THz (Q-factor ~ 2), indicating the strongly mixed "light-matter" nature of the cavity resonance. Bi-Lorentzian fitting of each reflectance spectrum were then performed to obtain the two experimental polariton frequencies ω_{UP} and ω_{LP} (fitting curves reported in the Supporting Information). In Figure 5(d,e) we report experimental (symbols) and simulated (segmented curves) polariton frequencies together with the bare cavity (undoped PQW) resonances. These two plots are not significantly different from each other, indicating that the absorption cross-section of single antennas is definitely smaller than $3s \times 3s$ and probably even smaller than $2s \times 2s$,[47] therefore we can confirm that we are spectroscopically studying the single-cavity properties. The minimum polariton splitting at the avoided-crossing point was used to estimate Ω_R. We calculated the average of the minimum splittings in the two samples at $s = 10\,\mu\text{m}$ (expected crossing point from simulations) and it gives $\Omega_R = 0.68 \pm 0.05$ THz. Finally we compared our experimental and simulated polariton dispersions with a theoretical model for the ultrastrong light-matter coupling (dipolar-coupling Hamiltonian[17]). The continuous grey curves in Figure 5(d,e) are calculated by solving the secular equation from Ref.[7,19,48]

$$(\omega^2 - {\omega_0}^2)(\omega^2 - \omega_c^2) = f_{\text{QW}}\omega_p^2\omega_c^2 \tag{3}$$

where $\omega_0 = 3.1$ THz is the measured ISBT from Figure 2(a), f_{QW} is the optical overlap factor (i.e. the cavity volume fraction occupied by the QWs as detailed below), $\omega_c = \frac{Ac}{s}$ is the simulated undoped-PQW cavity resonance from Figure 3(d) ($A \sim 0.1$ is a phenomenological proportionality constant and c is the light velocity in vacuum), and $\omega_p = \sqrt{\frac{f_{12}e^2 n_{2D}}{\varepsilon_0 \varepsilon m^* L_{QW}}}$ is the plasma frequency of the 2D-confined electron gas.[19,48] The best agreement between the experimental data points and the model is obtained for a plasma frequency $\omega_p = 2.6$ THz. For ideal PQWs, f_{12} can be taken close to 1 at all T (we use $f_{12} = 0.97$ to account for the few transitions with non-confined final states). Considering the sub-band state population at $T = 10$ K, only the ground state is significantly occupied, therefore we can write $L_{\text{QW}} = 21$

nm from the spatial extent of the ground-state wavefunction in Figure 1(e) and $f_{\mathrm{QW}} = L_{\mathrm{QW}}/(W+b) = 0.29$. We can now provide a global estimate from the theoretical model fitting to all data $\Omega_R = \omega_p\sqrt{f_{\mathrm{QW}}}/2 = 0.75$ THz, which quantifies the light-matter coupling strength in our system at 10 K. From the expression $\Omega_R = \sqrt{\frac{f_{12}e^2 n_{2D}}{\varepsilon_0 \varepsilon m^*(W+b)}}$, we can calculate $n_{2D} = 3.2\times10^{11}$ cm^{-2}, which is in good agreement with the independently measured spectral weight estimate in Figure 2 and with the Schrödinger-Poisson calculation of electron transfer from remote donors. The normalized coupling-strength ratio measured at the anti-crossing point from the theoretical polaritonic branches is $\frac{\Omega_R}{\omega_0} \simeq 0.24$, testifying the achievement of the ultrastrong coupling regime. Note that, in PQWs, Ω_R will only depend on T through n_{2D} and ω_0 is fairly T-independent, therefore the coupling regime should be almost T-independent up to room-T, as we now show.

Finally, in Figure 6 the temperature dependence of the polariton absorption spectra for one specific cavity array ($s = 12\,\mu$m, $P = 2s$) was explored. Reflection spectra in Figure 6(a) were taken while heating, without displacing the spot from the cavity array. A first observation (Figure 6(b)) is the presence of the upper polariton line almost unchanged between 300 and 10 K, with only a small redshift of ω_{UP} with decreasing T (blue triangles). As a matter of fact, we observe a blueshift of the undoped cavity resonance from 300 K to 10 K (orange triangles in Figure 6(b) and dotted curves in Figure 6(a)), explained by the decrease of the dielectric constant of Ge from ~ 16 to ~ 15 triggered by the widening of the Ge bandgap. We attribute the observed deviation of ω_{UP} from the expected blueshift (dashed red line) to a decrease of n_{2D} with decreasing $T < 100$ K, now sensitively measured through Eq. 1 from the measured coupling strength $2\Omega_R(T) = \omega_{\mathrm{UP}}(T) - \omega_{\mathrm{LP}}$ (where we have assumed $\omega_{\mathrm{LP}} = 2.1$ THz constant at all T). Starting from the estimate from Eq. 3 $n_{2D} = 3.2 \times 10^{11}$ cm^{-2} at 10 K, we get $n_{2D} = 3.5 \times 10^{11}$ cm^{-2} at 100 K. A decrease of $n_{2D}(T)$ with decreasing T is theoretically explained by the T-dependence of the relative energy position of confined states in the barriers and in the PQWs, which limits the electron transfer from the dopant impurities to the PQWs at low T. The latter effect is due to the

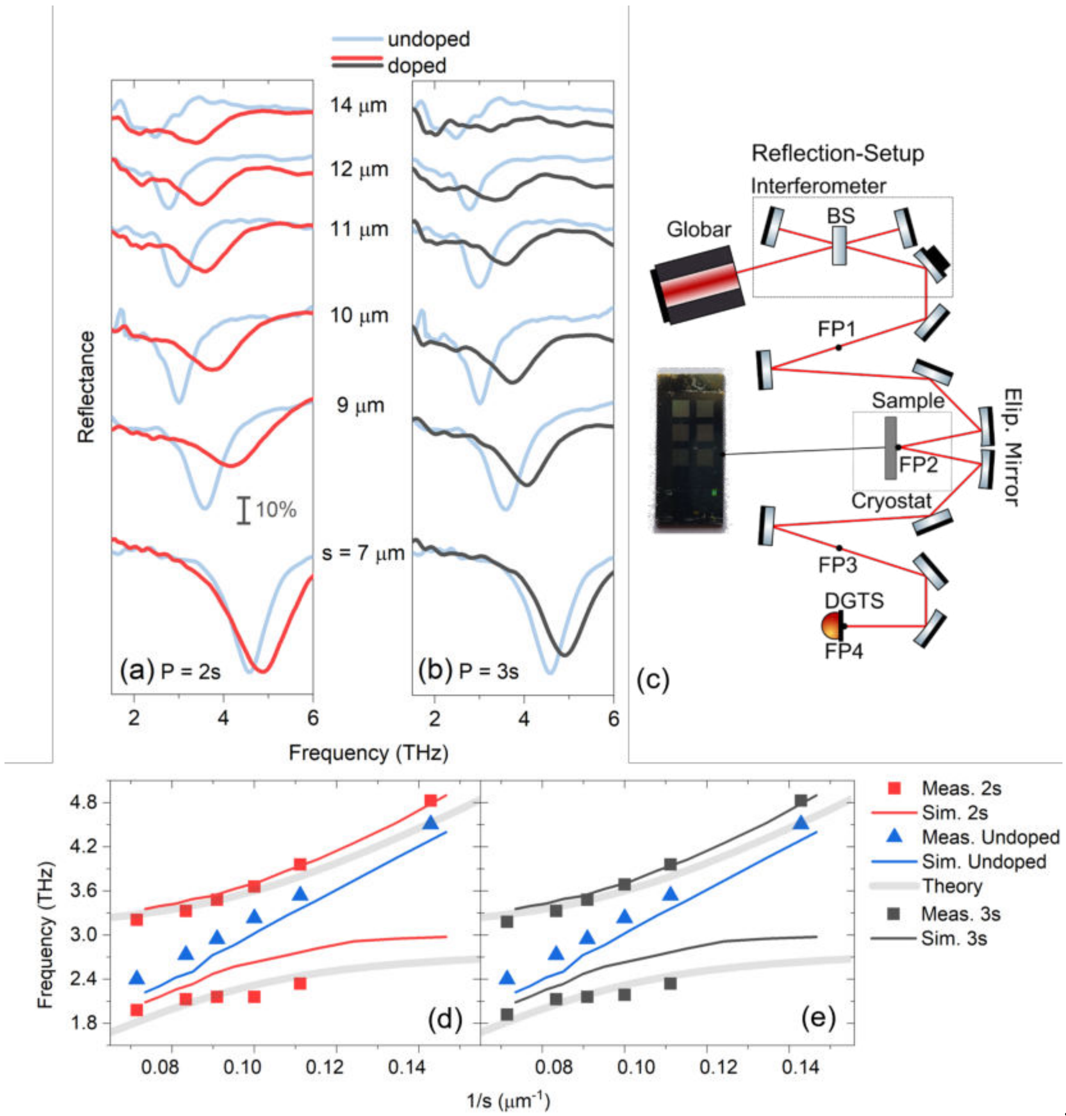

Figure 5: (a) reflection spectra of the cavity arrays with $P = 2s$ (red curves), the grey curves are the reflection spectra of identical cavities fabricated on a sample with undoped PWQs. (b) Reflection spectra of cavities filled with identical doped PQWs but $P = 3s$. (c) sketch of the custom de-magnifying reflection setup and picture of the fabricated sample chip with all cavity arrays (2×2 mm^2). (d, e) polariton dispersion as determined by a bi-Lorentzian fitting of the data in panels a, b respectively. The error bar for the polariton frequencies in a single fitting routine is smaller than the symbol size.

different thermal expansion coefficient of Ge and SiGe,[49] which can be precisely simulated as detailed in the Methods. A second observation is the decrease of the upper polariton linewidth $\Gamma_{\mathrm{UP}}(T)$ from 300 K to 100 K, highlighted in Figure 6(c). This behavior mirrors the $\Gamma_{\mathrm{ISBT}}(T)$ seen in Figure 2, indicating that the polariton linewidth is determined by the same intrinsic material mechanisms that define the ISBT linewidth.[50] As a consequence of line broadening, the lower polariton line goes below the detection threshold of our experiment above 200 K. Even if the lower polariton disappears from the spectra of Figure 6(a) above 200 K, the strong-coupling condition is clearly maintained up to 300 K, as seen from the 1 THz-offset of ω_{UP} (continuous red spectrum in Figure 6(a)) from ω_c measured in the undoped PQW sample (dotted red spectrum). This is at odds with observations in III-V material PQWs, where both polaritons merge to ω_c around 200 K and then disappear at room-T.[19] We can conclude that, in suitably designed and grown $\mathrm{Si}_{1-x}\mathrm{Ge}_x$ PQWs, Ω_R can be made almost independent on T up to 300 K. We have further verified this occurrence by measuring all cavities with different s at room-T: the offset of ω_{UP} from the corresponding ω_c is clearly observed for all cavities at room-T, decreasing with increasing detuning (decreasing s) as expected, see Supporting Information.

To summarize, from the spectroscopy data in Figure 6(a) the coupling parameters plotted in Figure 6(c) were retrieved, from which an experimental demonstration of the ultrastrong-coupling condition can be obtained at all T: it can be deduced that the normalized coupling-strength ratio Ω_R/ω_0 stays around 0.2, almost T-independent from 10 K to room-T. Note that this experimental estimate agrees very well with theory fitting to raw polartion dispersion data at 10 K in Figure 5(d-e). Rabi oscillations are overdamped as $\Omega_R/\Gamma_{\mathrm{UP}} \sim 0.5$ at room-T and $\Omega_R/\Gamma_{\mathrm{UP}} \sim 0.7$ at 100 K: here we take Γ_{UP} as a reasonable estimate of polariton lifetimes, which seems to be closely related to Γ_{ISBT}. The polariton quality factor is consistently lager than unity, i.e. $\omega_{\mathrm{UP}}/\Gamma_{\mathrm{UP}} = 2.4$ at room-T and $\omega_{\mathrm{UP}}/\Gamma_{\mathrm{UP}} = 3.6$ at 100 K, which makes the present microcavities usable in THz photonics applications e.g. as amplitude modulators.[51]

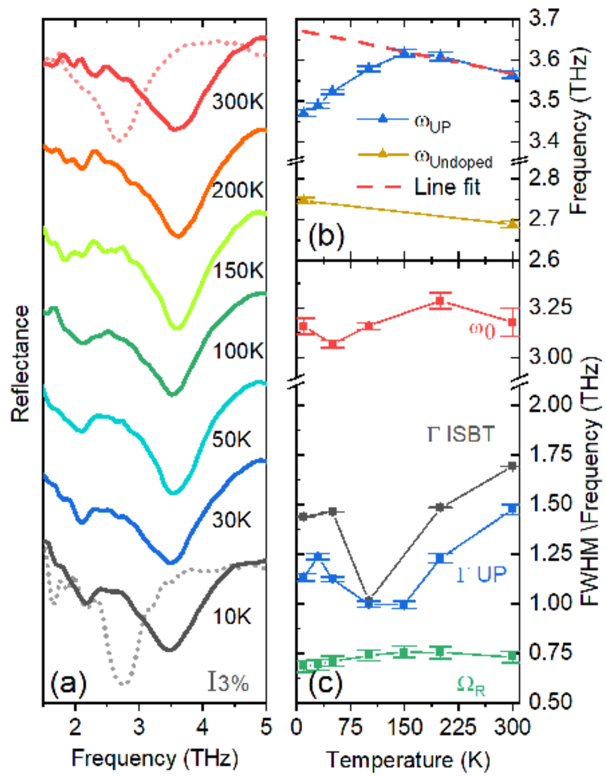

Figure 6: (a): temperature dependence of the reflectance of ultrastrongly coupled cavities with $s = 12\mu$m and $P = 2s$ (solid curves) and comparison with undoped cavities (dashed curves). (b): temperature dependence of the extracted upper polariton frequency compared to predictions based on the T-dependence of the dielectric constant of Ge and to the undoped sample (c): temperature dependence of: uncoupled intersubband resonance linewidth Γ_{ISBT}; upper polariton linewidth Γ_{UP}; intersubband resonance frequency ω_0; Rabi splitting Ω_R.

In conclusion, we have implemented the ultrastrong light-matter coupling between the intersub-band transitions and a microcavity in electron-doped group-IV ($Si_{1-x}Ge_x$) parabolic quantum wells, which present small effective mass of electrons and regular Fermi surface geometry in the conduction band, comparable to the typical ones of n-type III-V semiconductors. This implementation provides: 1) Almost temperature-independent light-matter coupling up to room-temperature at $\omega_0 = 3.1$ THz; 2) High values of the 2D electron density hence of the coupling, as testified by $\Omega_R/\omega_0 \simeq 0.2$; 3) Compatibility with silicon photonics foundry technology, and potentially with the silicon CMOS process, because we crucially show that, in the THz range, the typical gold mirrors of microcavities can be substituted by doped-semiconductor "plasmonic" mirrors. The present SiGe material platform will be relevant in future mainstream applications in quantum technology, where photon quantum states and integrated electronic circuits will have to interact on-chip. Due to both the CMOS compatibility of the PQW material and the rather large dimensions of the patch antennas in comparison to modern foundry processes, a further integration of the proposed system into an electrical controlled sensor or manipulator is viable. Using planarization steps all patch antennas could be electrically connected either at the 2DEG level, to read out the electron state by electrical transport measurements, and/or at the field-effect gate level, to populate or depopulate the PQW. This would not be possible with purely photonic or geometrical-plasmonic resonators.[52] In terms of progress in THz optoelectronics, the relevant outcome is that our approach can be easily extended up to 12 THz, while III-V compound semiconductors are inefficient above 5 THz due to optical phonon absorption in the reststrahlen band. In particularly, using rectangular quantum wells in similar cavities and tailoring the strong coupling condition, one should be able to develop ultrafast switches and saturable absorbers,[53] to be employed in laser science in the almost unexplored 5-12 THz range.

Methods

Quantum calculations

The electronic band structure, electron wave-functions, and ISBT absorption spectra of the investigated samples have been calculated self-consistently, relying on a multi-valley effective mass Schrödinger-Poisson solver. A detailed description of the model can be found in Ref.[39] For the T-dependence of n_{2D}, we have taken into account the presence, at energies comparable to the PQW sub-bands, of so-called Δ_2 states (situated along the $\Gamma - X$ line in k-space), confined in the barrier region. These levels limit the amount of charge transferred in the PQW sub-bands originating from the L-point band edge. Moreover, to tackle the T-dependence of the carrier density we have included in our model also the impact of the thermal strain induced by the difference in the thermal lattice expansion coefficient of Si and Ge. As a matter of fact, the thermal strain influences the energy separation between the Δ_2 and L sub-bands and provides n_{2D} monotonically decreasing with decreasing T.

Material growth

Samples were deposited by means of UHV CVD in a cold-wall reactor using ultrapure silane and germane without carrier gases. N-type doping was achieved by co-depositing phosphine. The active layer stack composed by 25 identical PQWs (thickness $W = 61$ nm) separated by $Si_{0.18}Ge_{0.82}$ barriers (thickness $b = 16$ nm) was grown on top of relaxed $Si_{1-x}Ge_x$ virtual substrate (VS) having low threading dislocation densities (TDD $= 3 \times 10^6$ cm^{-2}).[54] The VS growth on a Si(100) substrate leverages a reverse grading technique in which a Ge film is deposited directly on the Si substrate using a multi-temperature approach, followed by a compositional graded $Si_{1-x}Ge_x$ buffer layer.[37] The final Ge content in the buffer y matched the average Ge content of the active stack to ensure the strain compensation condition and avoid the plastic relaxation of the active region. In samples used to fabricate the microcavity arrays the last two micrometers of the VS were doped with a nominal P density $N_P = 1 \times 10^{19}$

cm^{-3}. The parabolic compositional profile $Si_{1-x}Ge_x$ with x in the range between $0.8 - 1$ of the wells was obtained by changing the SiH_4 gas flow and maintaining the GeH_4 one constant during the growth, using calibrated mass flow controllers. The deposition pressure varied consequently, and we estimated an average growth rate of 6 nm/min. The growth temperature for the active stack was set at 460°C. N-type modulation doping was achieved by co-depositing phosphine to a thickness of 5 nm in the center of the SiGe barriers. The nominal P density in the doped region of the barriers was 8×10^{17} cm^{-3}. The structural properties of the samples were evaluated by means STEM, XRD, and SIMS. STEM measurements have been performed using a FEI Titan microscope (FEI Company, Hillsboro, Oregon, USA) operating at 200 kV. It was equipped with aberration-corrected magnetic lenses to obtain electron probes with a diameter in the range of $1 - 2$ Å and beam currents of 200 pA. A CEOS CESCOR corrector was used to achieve a resolution of 0.8 Å . Images were recorded using a high-angle annular dark field (HAADF) detector (FEI Company, Hillsboro, Oregon, USA). Room-temperature XRD measurements were achieved by using a Rigaku SmartLab instrument with a rotating anode and line-focus geometry, featuring a Ge(400) $\times$ 2 channel-cut beam collimator. ToF-SIMS V from IONTOF was employed for the measurement of the compositional profiles. The depth profiles were acquired using $0.5 - 1$ keV a Cs^+ ion beam.

Infrared and Terahertz spectroscopy

Fourier-transform infrared (FTIR) spectroscopy was performed with a vacuum Bruker Vertex 70v spectrometer (Bruker, Ettlingen, Germany)) equipped with a helium-flow cryostat (Janis Research company, Woburn, Massachusetts (USA)), a wide-band silicon beamsplitter, a globar source and a pyroelectric detector with integrated preamplifier. For the ISBT measurements of Figure 2 performed in side-illuminated single-pass waveguide configuration, the lateral facets of our 2.5 mm long samples were cut at a 70° angle relative to the growth plane, and the top surface close to the QW stack was coated with a metal bilayer (Ti/Au 10 nm/80 nm), to align the electric field of the radiation propagating through the active region almost parallel to the ISBT dipole moment (i.e., TM polarized). The dichroic transmission spectra $T(\omega) = T_{TM}(\omega)/T_{TE}(\omega)$ were measured with a computer-controlled wire-grid polarizer, ensuring that polarization-independent spectral features unrelated to ISB transitions were suppressed. For the dielectric function determination of Figure 3, a quasi-normal incidence setup was employed, with incidence angle around 10° and a gold-coated surface as reference for determining the absolute reflectance $R(\omega)$. The latter quantity was processed via Kramers-Kronig tranformations, using a Hagen-Rubens extrapolation for $\omega \to 0$ and a Drude-Lorentz extrapolation beyond the non-transparency range above the plasma edge for $\omega \to \infty$. The resulting complex dielectric function $\tilde{\epsilon}$ is calculated from the complex reflectance $\tilde{r} = R(\omega) \cdot e^{i\phi(\omega)}$ via the standard Fresnel formulas. For the cavity measurements of Figures 5 ad 6 a high-numerical aperture reflectance setup was built using ellipsoidal mirrors with magnification factor $\times$ 3. The baseline-corrected reflectance of the cavity arrays was measured by using the bare doped-Ge ground plane as the reference. The cryostat cold finger was displaced vertically with a vacuum manipulator to change the spot position from a cavity array to another and to the reference during the same cryogenic cycle. 4096 scans at 10 kHz scanning speed and spectral resolution of 4 cm^{-1} were averaged for each cavity. Longer acquisition times did not lead to better signal-to-noise ratio below 30 cm^{-1} probably due to the $1/f$ noise of the DTGS detector.

Electromagnetic simulations

The finite element simulations have been carried out with CST microwave studio® employing the frequency domain solver. The highly doped mirror layer has been modeled with a user-defined dispersion employing the measured dielectric function data reported in Figure 3(b). The intersubband resonance has been modeled with the dielectric function from Ref.[46] and the metal is lossy gold from CST library.

Device fabrication

In a first step the metal patches were produced via electron beam evaporation and a lift-off process using an electron beam lithography (EBL) (Raith VOYAGER) and PMMA (Poly methyl methacrylate) as resist. First 10 nm Ti were evaporated functioning as an adhesion layer directly followed by 80 nm of Au to form the top side mirror. The lift-off was performed without an ultra sonic bath to avoid damages to the mirrors. After a second EBL step the etching of the microcvavity was performed by an inductively coupled plasma - reactive ion etching (ICP-IRE) SF_6-Ar step.

References

Acknowledgement

The Authors would like to acknowledge detailed discussions with Raffaele Colombelli.

G. Scalari acknowledges SNF project 200021–212735 for financial support.

M. De Seta, M. Ortolani and S. Cibella acknowledge support from Italian MIUR grant PRIN 2022 "Strong light-matter coupling manipulation in SiGe quantum wells at terahertz frequencies" CUP F53D23001190006.

Supporting Information Available

Supporting Information for Publication contain: Fitting curves to the reflectance spectra in Figure 5; fitting curves to the TM/TE measurements in Figure 2; fitting curves to the temperature depended measurements Figure 6; Reflectance spectra at room-temperature for all values of s for both doped and undoped PQWs; detailed procedures for the determination of n_{2D} from experiment and theory.

References

(1) Forn-Díaz, P.; Lamata, L.; Rico, E.; Kono, J.; Solano, E. Ultrastrong coupling regimes of light-matter interaction. *Rev. Mod. Phys.* **2019**, *91*, 025005.

(2) Mi, X.; Cady, J. V.; Zajac, D. M.; Deelman, P. W.; Petta, J. R. Strong coupling of a single electron in silicon to a microwave photon. *Science* **2017**, *355*, 156–158.

(3) Hou, J. T.; Liu, L. Strong Coupling between Microwave Photons and Nanomagnet Magnons. *Phys. Rev. Lett.* **2019**, *123*, 107702.

(4) Bayer, A.; Pozimski, M.; Schambeck, S.; Schuh, D.; Huber, R.; Bougeard, D.; Lange, C. Terahertz Light–Matter Interaction beyond Unity Coupling Strength. *Nano Letters* **2017**, *17*, 6340–6344, PMID: 28937772.

(5) Rajabali, S.; Markmann, S.; Jöchl, E.; Beck, M.; Lehner, C. A.; Wegscheider, W.; Faist, J.; Scalari, G. An ultrastrongly coupled single terahertz meta-atom. *Nature Communications* **2022**, *13*, 2528.

(6) Todorov, Y.; Andrews, A. M.; Sagnes, I.; Colombelli, R.; Klang, P.; Strasser, G.; Sirtori, C. Strong Light-Matter Coupling in Subwavelength Metal-Dielectric Microcavities at Terahertz Frequencies. *Phys. Rev. Lett.* **2009**, *102*, 186402.

(7) Geiser, M.; Castellano, F.; Scalari, G.; Beck, M.; Nevou, L.; Faist, J. Ultrastrong coupling regime and plasmon polaritons in parabolic semiconductor quantum wells. *Physical Review Letters* **2012**, *108*, 106402.

(8) Huck, C.; Vogt, J.; Neuman, T.; Nagao, T.; Hillenbrand, R.; Aizpurua, J.; Pucci, A.; Neubrech, F. Strong coupling between phonon-polaritons and plasmonic nanorods. *Opt. Express* **2016**, *24*, 25528–25539.

(9) Cortese, E.; Tran, N.-L.; Manceau, J.-M.; Bousseksou, A.; Carusotto, I.; Biasiol, G.;

Colombelli, R.; De Liberato, S. Excitons bound by photon exchange. *Nature Physics* **2021**, *17*, 31–35.

(10) Baumberg, J. J.; Aizpurua, J.; Mikkelsen, M.; Smith, D. R. Extreme nanophotonics from ultrathin metallic gaps. *Nature Materials* **2019**, *7*, 668–678.

(11) Chikkaraddy, R.; de Nijs, B.; Benz, F.; Barrow, S.; Scherman, O.; Rosta, E.; Demetriadou, A.; Fox, P.; Hess, O.; Baumberg, J. Single-molecule strong coupling at room temperature in plasmonic nanocavities. 2016.

(12) Muller, E. A.; Pollard, B.; Bechtel, H. A.; Adato, R.; Etezadi, D.; Altug, H.; Raschke, M. B. Nanoimaging and control of molecular vibrations through electromagnetically induced scattering reaching the strong coupling regime. *ACS photonics* **2018**, *5*, 3594–3600.

(13) Anappara, A. A.; Tredicucci, A.; Biasiol, G.; Sorba, L. Electrical control of polariton coupling in intersubband microcavities. *Applied Physics Letters* **2005**, *87*.

(14) Scalari, G.; Maissen, C.; Turcinkova, D.; D.Hagenmuller; Liberato, S.; Ciuti, C.; Reichl, C.; Schuh, D.; Wegscheider, W.; Beck, M.; Faist, J. Ultrastrong coupling of the cyclotron transition of a two-dimensional electron gas to a THz metamaterial. 2012.

(15) Zhang, Q.; Lou, M.; Li, X.; Reno, J. L.; Pan, W.; Watson, J. D.; Manfra, M. J.; Kono, J. Collective non-perturbative coupling of 2D electrons with high-quality-factor terahertz cavity photons. *Nature Physics* **2016**, *12*, 1005.

(16) Baydin, A.; Manjappa, M.; Mishra, S. S.; Xu, H.; Tay, F.; Kim, D.; Hernandez, F. G. G.; Rappl, P. H. O.; Abramof, E.; Singh, R.; Kono, J. Deep-Strong Coupling between Cavity Photons and Terahertz TO Phonons in PbTe. CLEO 2023. 2023; p FF3D.2.

(17) Ciuti, C.; Bastard, G.; Carusotto, I. Quantum vacuum properties of the intersubband cavity polariton field. *Phys. Rev. B* **2005**, *72*, 115303.

(18) Wang, C.-F.; Habteyes, T. G.; Luk, T. S.; Klem, J. F.; Brener, I.; Chen, H.-T.; Mitrofanov, O. Observation of Intersubband Polaritons in a Single Nanoantenna Using Nano-FTIR Spectroscopy. *Nano Letters* **2019**, *19*, 4620–4626.

(19) Goulain, P.; Deimert, C.; Jeannin, M.; Pirotta, S.; Pasek, W. J.; Wasilewski, Z.; Colombelli, R.; Manceau, J.-M. THz Ultra-Strong Light–Matter Coupling up to 200 K with Continuously-Graded Parabolic Quantum Wells. *Advanced Optical Materials* **2023**, *11*, 2202724.

(20) Anappara, A. A.; De Liberato, S.; Tredicucci, A.; Ciuti, C.; Biasiol, G.; Sorba, L.; Beltram, F. Signatures of the ultrastrong light-matter coupling regime. *Phys. Rev. B* **2009**, *79*, 201303.

(21) John, V.; Borsoi, F.; György, Z.; Wang, C.-A.; Széchenyi, G.; van Riggelen-Doelman, F.; Lawrie, W. I. L.; Hendrickx, N. W.; Sammak, A.; Scappucci, G.; Pályi, A.; Veldhorst, M. Bichromatic Rabi Control of Semiconductor Qubits. *Phys. Rev. Lett.* **2024**, *132*, 067001.

(22) Askenazi, B.; Vasanelli, A.; Delteil, A.; Todorov, Y.; Andreani, L. C.; Beaudoin, G.; Sagnes, I.; Sirtori, C. Ultra-strong light–matter coupling for designer Reststrahlen band. *New Journal of Physics* **2014**, *16*, 043029.

(23) Dicke, R. H. Coherence in Spontaneous Radiation Processes. *Phys. Rev.* **1954**, *93*, 99–110.

(24) Dini, D.; Köhler, R.; Tredicucci, A.; Biasiol, G.; Sorba, L. Microcavity Polariton Splitting of Intersubband Transitions. *Phys. Rev. Lett.* **2003**, *90*, 116401.

(25) Todorov, Y.; Tosetto, L.; Delteil, A.; Vasanelli, A.; Sirtori, C.; Andrews, A.; Strasser, G. Polaritonic spectroscopy of intersubband transitions. *Physical Review B* **2012**, *86*, 125314.

(26) Todorov, Y.; Sirtori, C. Few-Electron Ultrastrong Light-Matter Coupling in a Quantum LC Circuit. *Phys. Rev. X* **2014**, *4*, 041031.

(27) Delteil, A.; Vasanelli, A.; Todorov, Y.; Palma, C. F.; St-Jean, M. R.; Beaudoin, G.; Sagnes, I.; Sirtori, C. Charge-Induced Coherence between Intersubband Plasmons in a Quantum Structure. *Phys. Rev. Lett.* **2012**, *109*, 246808.

(28) Malerba, M.; Ongarello, T.; Paulillo, B.; Manceau, J.-M.; Beaudoin, G.; Sagnes, I.; De Angelis, F.; Colombelli, R. Towards strong light-matter coupling at the single-resonator level with sub-wavelength mid-infrared nano-antennas. *Applied Physics Letters* **2016**, *109*, 021111.

(29) Sarma, R.; Nookala, N.; Reilly, K. J.; Liu, S.; de Ceglia, D.; Carletti, L.; Goldflam, M. D.; Campione, S.; Sapkota, K.; Green, H.; others Strong coupling in all-dielectric intersubband polaritonic metasurfaces. *Nano Letters* **2020**, *21*, 367–374.

(30) Gillibert, R.; Malerba, M.; Spirito, D.; Giliberti, V.; Li, L.; Davies, A. G.; Linfield, E. H.; Baldassarre, L.; Colombelli, R.; Ortolani, M. Nanospectroscopy of a single patch antenna strongly coupled to a mid-infrared intersubband transition in a quantum well. *Applied Physics Letters* **2020**, *117*, 101104.

(31) Malerba, M.; Sotgiu, S.; Schirato, A.; Baldassarre, L.; Gillibert, R.; Giliberti, V.; Jeannin, M.; Manceau, J.-M.; Li, L.; Davies, A. G.; Linfield, E. H.; Alabastri, A.; Ortolani, M.; Colombelli, R. Detection of Strong Light–Matter Interaction in a Single Nanocavity with a Thermal Transducer. *ACS Nano* **2022**, *16*, 20141–20150, PMID: 36399696.

(32) Dietze, D.; Andrews, A.; Klang, P.; Strasser, G.; Unterrainer, K.; Darmo, J. Ultrastrong coupling of intersubband plasmons and terahertz metamaterials. *Applied Physics Letters* **2013**, *103*.

(33) Miller, R.; Gossard, A.; Kleinman, D.; Munteanu, O. Parabolic quantum wells with the G a A s- Al x Ga 1- x As system. *Physical Review B* **1984**, *29*, 3740.

(34) Deimert, C.; Goulain, P.; Manceau, J.-M.; Pasek, W.; Yoon, T.; Bousseksou, A.; Kim, N.; Colombelli, R.; Wasilewski, Z. Realization of harmonic oscillator arrays with graded semiconductor quantum wells. *Physical Review Letters* **2020**, *125*, 097403.

(35) Montanari, M.; Ciano, C.; Persichetti, L.; Corley, C.; Baldassarre, L.; Ortolani, M.; Di Gaspare, L.; Capellini, G.; Stark, D.; Scalari, G.; others THz intersubband absorption in n-type Si1- xGex parabolic quantum wells. *Applied Physics Letters* **2021**, *118*.

(36) Campagna, E.; Talamas-Simola, E.; Venanzi, T.; Berkmann, F.; Corley-Wiciak, C.; Nicotra, G.; Baldassarre, L.; Capellini, G.; Gaspare, L. D.; Virgilio, M.; Ortolani, M.; Seta, M. D. High-quality CMOS compatible n-type SiGe parabolic quantum wells for intersubband photonics at 2.5–5 THz. *Nanophotonics* **2024**,

(37) Capellini, G.; De Seta, M.; Busby, Y.; Pea, M.; Evangelisti, F.; Nicotra, G.; Spinella, C.; Nardone, M.; Ferrari, C. Strain relaxation in high Ge content SiGe layers deposited on Si. *Journal of Applied Physics* **2010**, *107*.

(38) Skibitzki, O.; Zoellner, M. H.; Rovaris, F.; Schubert, M. A.; Yamamoto, Y.; Persichetti, L.; Di Gaspare, L.; De Seta, M.; Gatti, R.; Montalenti, F.; others Reduction of threading dislocation density beyond the saturation limit by optimized reverse grading. *Physical Review Materials* **2020**, *4*, 103403.

(39) Busby, Y.; De Seta, M.; Capellini, G.; Evangelisti, F.; Ortolani, M.; Virgilio, M.; Grosso, G.; Pizzi, G.; Calvani, P.; Lupi, S.; others Near-and far-infrared absorption and electronic structure of Ge-SiGe multiple quantum wells. *Physical Review B* **2010**, *82*, 205317.

(40) Virgilio, M.; Sabbagh, D.; Ortolani, M.; Di Gaspare, L.; Capellini, G.; De Seta, M. Physical mechanisms of intersubband-absorption linewidth broadening in s-Ge/SiGe quantum wells. *Physical Review B* **2014**, *90*, 155420.

(41) Unuma, T.; Yoshita, M.; Noda, T.; Sakaki, H.; Akiyama, H. Intersubband absorption linewidth in GaAs quantum wells due to scattering by interface roughness, phonons, alloy disorder, and impurities. *Journal of applied physics* **2003**, *93*, 1586–1597.

(42) Todorov, Y. Dipolar quantum electrodynamics of the two-dimensional electron gas. *Physical Review B* **2015**, *91*, 125409.

(43) Frigerio, J. et al. Tunability of the dielectric function of heavily doped germanium thin films for mid-infrared plasmonics. *Phys. Rev. B* **2016**, *94*, 085202.

(44) Berkmann, F.; Steuer, O.; Ganss, F.; Prucnal, S.; Schwarz, D.; Fischer, I. A.; Schulze, J. Sharp MIR plasmonic modes in gratings made of heavily doped pulsed laser-melted Ge1-xSnx. *Opt. Mater. Express* **2023**, *13*, 752–763.

(45) Feuillet-Palma, C.; Todorov, Y.; Steed, R.; Vasanelli, A.; Biasiol, G.; Sorba, L.; Sirtori, C. Extremely sub-wavelength THz metal-dielectric wire microcavities. *Opt. Express* **2012**, *20*, 29121–29130.

(46) Załużny, M.; Nalewajko, C. Coupling of infrared radiation to intersubband transitions in multiple quantum wells: The effective-medium approach. *Phys. Rev. B* **1999**, *59*, 13043–13053.

(47) Langevin, D.; Verlhac, C.; Jaeck, J.; Abou-Hamdan, L.; Taupeau, E.; Fix, B.; Bardou, N.; Dupuis, C.; De Wilde, Y.; Haïdar, R.; others Experimental Investigation of the Thermal Emission Cross Section of Nanoresonators Using Hierarchical Poisson-Disk Distributions. *Physical Review Letters* **2024**, *132*, 043801.

(48) Todorov, Y.; Andrews, A. M.; Colombelli, R.; De Liberato, S.; Ciuti, C.; Klang, P.; Strasser, G.; Sirtori, C. Ultrastrong Light-Matter Coupling Regime with Polariton Dots. *Phys. Rev. Lett.* **2010**, *105*, 196402.

(49) Li, Y. S.; Nguyen, J. Tensilely strained Ge films on Si substrates created by physical vapor deposition of solid sources. *Scientific reports* **2018**, *8*, 16734.

(50) Manceau, J.-M.; Tran, N.-L.; Biasiol, G.; Laurent, T.; Sagnes, I.; Beaudoin, G.; De Liberato, S.; Carusotto, I.; Colombelli, R. Resonant intersubband polariton-LO phonon scattering in an optically pumped polaritonic device. *Applied Physics Letters* **2018**, *112*, 191106.

(51) Raab, J.; Mezzapesa, F. P.; Viti, L.; Dessmann, N.; Diebel, L. K.; Li, L.; Davies, A. G.; Linfield, E. H.; Lange, C.; Huber, R.; Vitiello, M. S. Ultrafast terahertz saturable absorbers using tailored intersubband polaritons. **2020**, 4290.

(52) *Nature Communications* **2020**, *11*.

(53) Jeannin, M.; Manceau, J.-M.; Colombelli, R. Unified Description of Saturation and Bistability of Intersubband Transitions in the Weak and Strong Light-Matter Coupling Regimes. *Phys. Rev. Lett.* **2021**, *127*, 187401.

(54) Talamas-Simola, E.; Montanari, M.; Corley-Wiciak, C.; Di Gaspare, L.; Persichetti, L.; Zöllner, M. H.; Schubert, M. A.; Venanzi, T.; Trouche, M. C.; Ortolani, M.; others Subnanometer control of the heteroepitaxial growth of multimicrometer-thick Ge/Si-Ge quantum cascade structures. *Physical Review Applied* **2023**, *19*, 014011.

TOC Graphic

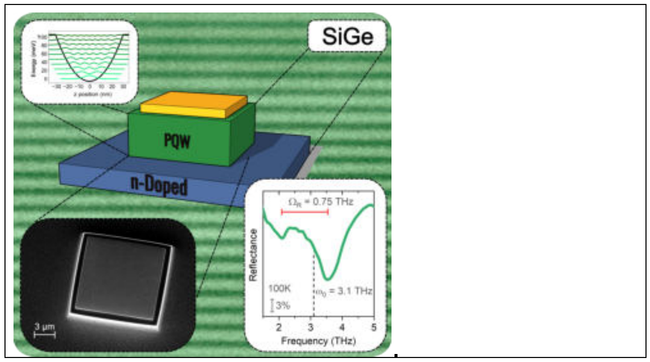
SiGe
PQW
n-Doped
3 μm
Ω_R = 0.75 THz
Reflectance
100K
3%
ω_0 = 3.1 THz
2
3
4
5
Frequency (THz)